Lithium Diffusion Pathways in 3R-Li$_x$TiS$_2$: A Combined Neutron Diffraction and Computational Study

Dennis Wiedemann,*,[†] Mazharul M. Islam,[‡] Suliman Nakhal,[†] Anatoliy Senyshyn,[§] Thomas Bredow,[‡] and Martin Lerch[†]

[†]Institut für Chemie, Technische Universität Berlin, Sekretariat C2, Straße des 17. Juni 135, 10623 Berlin, Germany

[‡]Mulliken Center for Theoretical Chemistry, Institut für Physikalische und Theoretische Chemie, Universität Bonn, Beringstraße 4, 53115 Bonn, Germany

[§]FRM II, Technische Universität München, Lichtenbergstraße 1, 85747 Garching b. München, Germany

S *Supporting Information*

ABSTRACT: Layered lithium transition-metal sulfides have long been discussed as early electrode materials for lithium-ion batteries. However, fundamental knowledge of lithium-ion migration in these solids is still lacking. In this study, we report on the diffusion dynamics in lithium-deficient high-temperature polymorphs of lithium titanium sulfides (3R-Li$_x$TiS$_2$; x = 0.7, 0.9) as analyzed using powder neutron diffractometry and density functional theory (DFT) climbing-image nudged-elastic-band (cNEB) calculations. Two classes of probable migration pathways have been identified from the scattering-length density distributions (filtered using the maximum-entropy method [MEM]) and the probability density functions (PDFs, modeled from anharmonic Debye−Waller factors): direct diffusion in the (001) plane as the major mechanism and indirect diffusion through adjacent tetrahedral voids as a minor mechanism. Calculated activation barriers agree well with one-particle potentials (OPPs) derived from measurements for Li$_{0.7}$TiS$_2$ (0.484[14] and 0.88[4] eV) but deviate for Li$_{0.9}$TiS$_2$. The discrepancy at low defect concentration is attributed to the failure of the OPP derivation and the different nature of the methods (space-time averaged vs individual-ion perspective). This work elucidates the pathways of lithium-ion diffusion in 3R-Li$_x$TiS$_2$ and points out pitfalls in established experimental/computational methods.

(001) in 3R-Li$_x$TiS$_2$
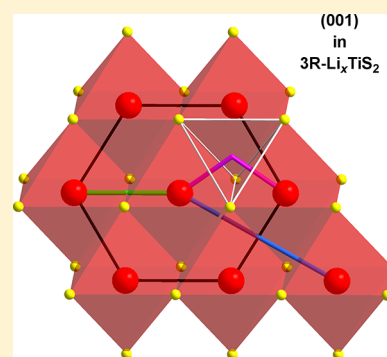
1. INTRODUCTION

In 1975, titanium disulfide was unambiguously characterized by Thompson et al. for the first time.[1] As a layered material, it has long been known to be a suitable host for small to medium-size entities like ammonia molecules and sodium and lithium ions.[2−4] The latter may easily be intercalated into the van der Waals gap between TiS$_2$ layers by chemical as well as electrochemical means. This had led to an early discussion of lithium titanium disulfide in terms of energy storage,[5] long before modern lithium-ion batteries and higher-voltage materials like LiCoO$_2$ were developed.[6] In spite of the great deal of work invested into the optimization of such batteries, fundamental knowledge of lithium-ion migration in these solids is still lacking. For this reason, we are researching two-dimensional lithium-ion diffusion in materials of the type Li$_x$MS$_2$ (M: transition metal), our main interest being the influence of the MS$_2$ framework (coordination polyhedra and anion stacking).

Two polymorphs of titanium disulfide have been synthesized and characterized so far: 1T-TiS$_2$ (CdI$_2$ type, space group: $P\bar{3}m1$) consists of S−Ti−S sandwich layers stacked in c direction (AB sequence of sulfide ions) that are held together by relatively weak van der Waals forces.[7] c-TiS$_2$ (Ti$_2$C type, space group: $Fd\bar{3}m$) is of the cubic-spinel type and may be

prepared by decupration of the thiospinel CuTi$_2$S$_4$.[8,9] Both polymorphs may be lithiated chemically (e.g., by suspending them in n-butyllithium solutions) to yield compounds of the compositions Li$_x$TiS$_2$ ($x \leq 1$).[10,11] The lithium ions are octahedrally coordinated between the S−Ti−S sandwich layers (see Figure 1) at the 16c position for 1T-LiTiS$_2$ (LiTiS$_2$ type, filled CdI$_2$-type structure)/c-LiTiS$_2$, respectively.[10] In 1989, Colbow et al. reported the synthesis of another polymorph at elevated temperatures (500 °C $\leq \vartheta \leq$ 900 °C): compared to the 1T phase, 3R-LiTiS$_2$ (NaCrS$_2$ type, space group: $R\bar{3}m$) exhibits a different stacking sequence of the sulfide layers (ABC in c direction, see Figure 1). Lithium-deficient 3R-Li$_x$TiS$_2$ phases were obtained for $0.4 \leq x \leq 1.0$, and lower lithium contents yielded 1T polymorphs only.[12]

In spite of the major interest in Li$_x$TiS$_2$ as a paradigmatic layered lithium conductor, our groups were the first to take a closer look at 3R-LiTiS$_2$. Our calculations have shown that it is metastable with respect to the 1T phase. After following a new synthesis route, full Rietveld refinements against powder X-ray diffraction data have allowed us to establish a complete
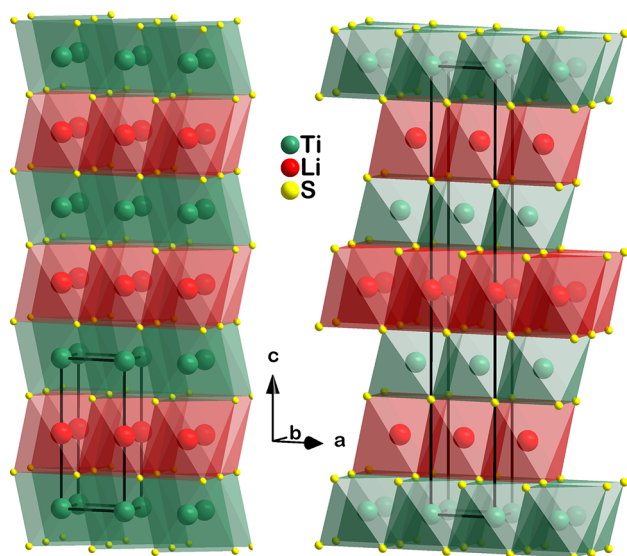
Figure 1. Crystal structures of 1T-LiTiS$_2$ (left) and 3R-LiTiS$_2$ (right). Ions represented with arbitrary radii; unit-cell edges shown as solid lines.

structural model.[13] Very recently, neutron diffraction experiments[14] as well as a nuclear magnetic resonance (NMR) study by Wilkening[15] have proven the model to be valid and have given deeper insight into the transformation between the 1T and the 3R polymorphs of Li$_x$TiS$_2$.

Lithium diffusion in battery materials has also become a subject of many theoretical studies.[16] The approaches range from pure geometrical considerations, e.g., via the Voronoi−Dirichlet partitioning scheme combined with bond-valence theory,[17] to first-principles quantum-chemisty methods, predominantly density functional theory (DFT), but also quantum Monte Carlo.[18] For Li$_x$TiS$_2$ compounds, a number of DFT studies exists. Electric field gradients and stability of lithium ions in tetrahedral and octahedral interstitials in 1T-Li$_x$TiS$_2$ were calculated at the hybrid DFT level and compared to experiments.[19] Lithium diffusion in TiS$_2$ nanotubes was studied by Ceder et al.[20] The mixed anion effect was studied theoretically and experimentally for Li$_x$TiS$_y$Se$_{1−y}$.[21] The mechanisms of lithium migration were studied by DFT for spinel c-Li$_x$TiS$_2$[22] and 1T-Li$_x$TiS$_2$.[23,24]

In this work, we present the evaluation of neutron diffraction experiments with powders of 3R-Li$_x$TiS$_2$ (x = 0.7, 0.9) as well as DFT climbing-image nudged-elastic-band (cNEB) calculations. From experimental data, *probability density functions* (PDFs) and *effective one-particle potentials* (OPPs), elucidating lithium migration pathways and energetics, are derived. Finally, the limits of the method employed and the comparability to computational results are discussed.

2. EXPERIMENTAL SECTION

2.1. Materials and Syntheses. 1T-Li$_x$TiS$_2$ samples (x = 0.7 and 0.9) were prepared and analyzed as published before.[14] When being heated from 400 to 600 °C, the material reversibly transformed from the 1T to the 3R phase, as evidenced by neutron diffractograms.

2.2. Powder Neutron Diffractometry. *2.2.1. Diffraction Experiments.* Diffraction experiments were conducted at the neutron source FRM II (MLZ, Garching b. München) using the high-resolution powder diffractometer SPODI with

Ge(551)-monochromated neutrons (λ = 154.829 pm) in Debye−Scherrer geometry.[25] The powder samples were compacted in a niobium cylinder (d = 8 mm, h = 15 mm) and mounted in a vacuum high-temperature furnace. Measurements were carried out at 600 and 700 °C with an exposure time of 5 h each. Data were recorded with an array of 80 position-sensitive ^{3}He tubes ($2\theta_{max}$ = 160°, effective height: 300 mm) and reduced using a variable-height algorithm as implemented in the in-house parser,[25] yielding a final range of $0.95° \leq 2\theta \leq 151.90°$ with $\Delta(2\theta) = 0.05°$.

2.2.2. Model Refinement. As a starting point, a known model for NaCrS$_2$ from the Inorganic Crystal Structure Database (ICSD) was imported and adjusted to reflect the actual cell parameters and contents.[26] Models were then refined with JANA2006 against 2θ data analytically corrected for absorption (cylindrical sample) using the full-matrix least-squares algorithm.[27]

Regions containing the very strong reflections of the niobium container or weak nonoverlapping reflections, caused by a small amount of TiO$_2$ (rutile type) in Li$_{0.7}$TiS$_2$ (w < 0.01; at ca. 36.1°, 41.3°, 69.1°, and 77.7°) and by a small amount of Li$_x$TiO$_2$ (NaCl type) in Li$_{0.9}$TiS$_2$ ($w \ll 0.05$; at ca. 31.2°, 37.5°, 43.1°, 76.0°, and 106.2°), were excluded from the refinement. The background proved to be complex because of the container reflections. Thus, it had to be defined manually with 35−39 points that were interpolated using five Legendre polynomials with refined coefficients. Peak profiles were fitted with a pseudo-Voigt function following the Thompson−Cox−Hastings approach.[28] Asymmetry was corrected for using the two-term Bérar−Baldinozzi method.[29] The approach of March and Dollase was employed to model a preferred orientation in (001).[30,31]

All atoms were refined with anisotropic atomic displacement parameters. Additionally, the lithium atom was modeled anharmonically with terms up to the order of four. Only statistically meaningful tensorial coefficients ($D_{jklm} \geq 3\sigma[D_{jklm}]$) were kept in the refinement. As a strong correlation between B_{11} and D_{1111} occurred, the former was fixed at the final stage for appropriate PDF error estimation.

2.2.3. Calculation of PDFs and OPPs. Maps of the PDF illustrating time- and space-averaged atomic distributions were calculated using the facilities of JANA2006 that include a Monte Carlo method (1000 iterations) for error handling.[32] Assuming independent single-particle motion governed by Boltzmann statistics, effective OPP barriers along proposed paths were calculated within JANA2006. OPP maps for visualization were calculated with the in-house program CALCOPP.[33]

Results were visualized using DIAMOND (structures),[34] VESTA (isosurface plots),[35] and QTIPLOT (contour plots).[36]

2.3. MEM Analyses. As interoperation between JANA2006 and programs implementing maximum-entropy methods (MEM) is rather complex, full Rietveld refinements with FULLPROF were used to extract structure factors from neutron diffractograms.[37] Dividing the unit cell into 128 × 128 × 128 pixels, MEM analyses of scattering-length density was conducted with the program PRIMA using 71 structure factors for each phase.[38]

2.4. Computational Methods. Bulk and defect properties of 3R-Li$_x$TiS$_2$ (x = 1.0, 0.92, 0.67) were obtained with periodic calculations at the DFT level. The Perdew−Burke−Ernzerhof (PBE) functional,[39,40] based on the generalized gradient approximation (GGA), was used as implemented in the plane-wave program VASP.[41−43] The projector-augmented

Table 1. Details of the Rietveld Refinements

	3R-Li$_{0.7}$TiS$_2$		3R-Li$_{0.9}$TiS$_2$	
ϑ/°C	600	700	600	700
space group	$R\bar{3}m$ (no. 166)	$R\bar{3}m$ (no. 166)	$R\bar{3}m$ (no. 166)	$R\bar{3}m$ (no. 166)
crystal system	trigonal	trigonal	trigonal	trigonal
M_r	116.9	116.9	118.2	118.2
a/pm	349.902(7)	349.658(8)	352.138(8)	353.131(8)
c/pm	1864.98(6)	1865.29(7)	1855.88(6)	1860.90(6)
V/10^6 pm^3	197.741(12)	197.499(13)	199.300(9)	200.967(13)
Z	3	3	3	3
ρ_{calc}/g cm^{-3}	2.944	2.9476	2.9557	2.9311
$wR_p{}^a$	0.0263	0.0324	0.0264	0.0260
$wR_{exp}{}^a$	0.0225	0.0312	0.0215	0.0214
R_B	0.0277	0.0291	0.0211	0.0296
S^b	1.17	1.04	1.23	1.22
$R_F{}^b$	0.0423	0.0366	0.0261	0.0296
CSD no.	429110	429111	429112	429113

$^a w = [\sigma^2(F_0) + (0.01F_0)^2]^{-1}$. ^{b}For all reflections.

wave (PAW) method was used for the core−electron representation.[44,45] We used a converged value of the energy cutoff E_{cut} = 420 eV, as optimized for 3R-LiTiS$_2$. The integration in reciprocal space was performed with a 15 × 15 × 3 Monkhorst−Pack grid,[46] as the energy convergence was achieved at 10^{-6} eV per cell with these values. In order to consider the effect of dispersion forces due to the presence of van der Waals gaps between the sulfide layers, we used recently proposed DFT-D methods based on D3[47] and D3BJ[48] correction schemes.

The defective structures were simulated using Li$_{12}$Ti$_{12}$S$_{24}$ and Li$_{27}$Ti$_{27}$S$_{54}$ supercells. The transition-state search for the migration processes was conducted with the cNEB method as implemented in VASP.[49] Vibrational analysis calculations were performed to verify the true local-minimum or saddle-point character of the optimized geometries. No imaginary frequency was obtained for the local-minimum structures, whereas one imaginary frequency was observed for the transition-state structures.

3. RESULTS AND DISCUSSION

3.1. Powder Neutron Diffraction Studies. *3.1.1. Structure and Model Refinement.* The lithium-deficient lithium titanium disulfides 1T-Li$_x$TiS$_2$ (being mixed-valence compounds of the actual formula Li$_x$Ti$^{III}_x$Ti$^{IV}_{1-x}$S$_2$) with x = 0.7 and 0.9 were readily accessible via chemical lithiation of 1T-LiS$_2$. To our surprise, the 1T phases transformed reversibly into the 3R phases during neutron diffractometry when heated from 400 to 600 °C. Nevertheless, this finding is in tune with antecedent literature stating that the 3R phase is destabilized by lower lithium content in favor of the 1T phase at low temperatures but may be present at higher ones.[12]

Using the diffractograms acquired for 3R-Li$_x$TiS$_2$ (x = 0.7 and 0.9) at 600 and 700 °C, models were refined with the Rietveld method (see Figures S1−S4, Supporting Information). The inevitable exclusion of the very strong niobium container reflections left a complex background that had to be modeled with manually chosen points. The utmost care has to be taken if their heights are not refinable (as with JANA2006), as the background choice is strongly correlated with the atomic displacement parameters. In each refinement, profile matching was conducted at first. As soon as all profile parameters converged to sensible values, individual atoms were included,

and their positions and isotropic displacement parameters were refined. Considerable effects of a well-known preferred orientation in the (001) plane were found and modeled. As expected for transmission measurements with plate-like crystallites, March−Dollase distribution parameters refined to values of r > 1. In the next step, anisotropic displacement parameters (ADPs) were introduced for all atoms. Finally, the lithium atom was modeled anharmonically with terms up to the order of four, adding up to six displacement parameters (two of second order, none of third order, four of fourth order heeding symmetry restrictions). For this purpose, the Gram−Charlier expansion of the Debye−Waller factor (DWF) was used (**h**: diffraction vector with components h_j, h_k, h_l, and h_m; T_h: anisotropic Gaussian DWF; C_{jkl} and D_{jklm}: third- and fourth-order anharmonic tensorial coefficients, respectively)[50]

$$T(\mathbf{h}) = T_h(\mathbf{h})\left[1 + (2\pi i)^3 \sum_{j,k,l} C_{jkl} \frac{h_j h_k h_l}{3!} \right.$$
$$\left. + (2\pi i)^4 \sum_{j,k,l,m} D_{jklm} \frac{h_j h_k h_l h_m}{4!} \right]$$

The global parameters of the refinement procedure are summarized in Table 1. All models are of a good quality as indicated by residuals R and goodness of fit S. Owing to thermal expansion, the final cell parameters a and, especially, c are somewhat larger at 600 and 700 °C than previously measured at room temperature[12] or computed for x = 0.7 and 0.9 (see below). The expected trends are however nicely reproduced: a increases, whereas c decreases with x in the high-content range. Interestingly, a slightly decreases when raising the temperature from 600 to 700 °C in 3R-Li$_{0.7}$TiS$_2$, but this effect has not been looked into more deeply.

Tables 2 and 3 list the final atomic parameters and bond geometries for the examined compounds. The fractional z coordinate of the sulfide ion $z(S1)$ does not change by more than 3σ with temperature and shifts only slightly with lithium content. As expected, the equivalent isotropic displacement parameters B_{eq} as well as the individual components B_{ij} of the anisotropic displacement tensor (most prominently B_{33}) increase with rising temperature. Surprisingly, their central values decrease slightly for Li1 in Li$_{0.9}$TiS$_2$ when heating from

Table 2. Final Atomic Parameters

atom	site	x	y	z	displacement parameters
3R-Li$_{0.7}$TiS$_2$ at 600 °C					
Li1	3b	0	0		$B_{eq} = 11.0(5)$ Å^2
					$B_{11} = 0.37(2)$ Å^2, $B_{33} = 0.0042(7)$ Å^2
					$D_{1111} = 11(2) \times 10^{-4}$, $D_{1113} = 0$, $D_{1133} = 0.078(19) \times 10^{-4}$, $D_{3333} = 0$
Ti1	3a	0	0	0	$B_{eq} = 2.56(9)$ Å^2
					$B_{11} = 0.0662(16)$ Å^2, $B_{33} = 0.00202(17)$ Å^2
S1	6c	0	0	0.2571(2)	$B_{eq} = 2.49(8)$ Å^2
					$B_{11} = 0.0536(13)$ Å^2, $B_{33} = 0.00254(17)$ Å^2
3R-Li$_{0.7}$TiS$_2$ at 700 °C					
Li1	3b	0	0		$B_{eq} = 12.5(7)$ Å^2
					$B_{11} = 0.38(3)$ Å^2, $B_{33} = 0.0070(9)$ Å^2
					$D_{1111} = 9(2) \times 10^{-4}$, $D_{1113} = 0$, $D_{1133} = 0.14(3) \times 10^{-4}$, $D_{3333} = 0$
Ti1	3a	0	0	0	$B_{eq} = 3.11(12)$ Å^2
					$B_{11} = 0.071(2)$ Å^2, $B_{33} = 0.0030(3)$ Å^2
S1	6c	0	0	0.2568(3)	$B_{eq} = 2.76(10)$ Å^2
					$B_{11} = 0.0591(15)$ Å^2, $B_{33} = 0.0028(2)$ Å^2
3R-Li$_{0.9}$TiS$_2$ at 600 °C					
Li1	3b	0	0		$B_{eq} = 5.8(3)$ Å^2
					$B_{11} = 0.155(7)$ Å^2, $B_{33} = 0.0042(5)$ Å^2
					$D_{1111} = 0$, $D_{1113} = -0.05(2) \times 10^{-4}$, $D_{1133} = 0.011(4) \times 10^{-4}$, $D_{3333} = 0$
Ti1	3a	0	0	0	$B_{eq} = 2.24(12)$ Å^2
					$B_{11} = 0.062(2)$ Å^2, $B_{33} = 0.0015(3)$ Å^2
S1	6c	0	0	0.2554(2)	$B_{eq} = 2.15(11)$ Å^2
					$B_{11} = 0.0507(16)$ Å^2, $B_{33} = 0.0020(3)$ Å^2
3R-Li$_{0.9}$TiS$_2$ at 700 °C					
Li1	3b	0	0		$B_{eq} = 5.4(3)$ Å^2
					$B_{11} = 0.153(7)$ Å^2, $B_{33} = 0.0034(5)$ Å^2
					$D_{1111} = 0$, $D_{1113} = -0.06(2) \times 10^{-4}$, $D_{1133} = 0$, $D_{3333} = 0$
Ti1	3a	0	0	0	$B_{eq} = 2.44(12)$ Å^2
					$B_{11} = 0.069(3)$ Å^2, $B_{33} = 0.0016(3)$ Å^2
S1	6c	0	0	0.2562(3)	$B_{eq} = 2.27(11)$ Å^2
					$B_{11} = 0.0542(16)$ Å^2, $B_{33} = 0.0020(3)$ Å^2

Table 3. Bond Lengths (in Picometers) and Bond Angles (in Degrees)

	3R-Li$_{0.7}$TiS$_2$		3R-Li$_{0.9}$TiS$_2$	
ϑ/°C	600	700	600	700
Li1–S1	263.1(2)	262.7(3)	261.6(3)	263.3(3)
Ti1–S1	247.1(2)	247.2(3)	249.5(2)	249.3(3)
S1–Li1–S1	83.35(7)	83.44(9)	84.59(7)	84.22(9)
	96.65(7)	96.56(9)	95.41(7)	95.78(9)
	180.0(5)	180.0(5)	180.0(5)	180.0(5)
S1–Ti1–S1	89.84(7)	90.00(9)	89.76(7)	89.83(9)
	90.16(7)	90.00(9)	90.24(7)	90.17(9)
	180.0(5)	180.0(5)	180.0(5)	180.0(5)

600 to 700 °C, although their error intervals overlap. Throughout all measurements, B_{eq} is distinctly larger for the lithium ion than for the other ions. This indicates dynamic

effects, namely, lithium migration, in a much more static framework of titanium and sulfide ions. Strikingly, for $x = 0.9$, B_{eq} is less than half as large as for $x = 0.7$. The partial lack of lithium defects that are targets for migration seems to hinder diffusion, the lithium ions becoming thus more strongly localized.

Representative refinements have been performed to test if lithium had evaporated (free lithium occupancy), if lithium ions partly occupy tetrahedral voids (distribution with fixed occupancy sum), and if anharmonic displacement terms of higher order are appropriate. As none of the changes led to improvements and physically sensible results at the same time, we stuck to our initial model. Furthermore, no hint at lithium ordering was found.

Inspection of Fourier and difference-Fourier maps of the scattering-length densities showed the model to be adequate around the atom positions. Near the centers of the tetrahedral voids adjacent to the lithium layer, however, small regions of negative scattering-length density were found (exemplarily, see Figure 2 for Li$_{0.7}$TiS$_2$ at 700 °C) that could not be satisfactorily
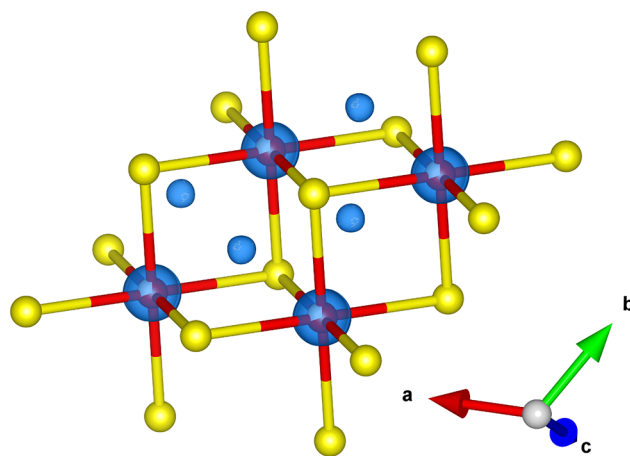

Figure 2. Detail of the (observed) Fourier map of Li$_{0.7}$TiS$_2$ at 700 °C showing only negative scattering-length density in and near the lithium layer. Yellow: sulfide ions, red: lithium ions, both with arbitrary radii; blue: isosurface for $\rho_b = -1.00$ fm $\times$ 10^{-6} pm^{-3}.

modeled. As lithium and titanium are both elements with negative scattering lengths, but lithium ions are the only mobile ones in the considered compounds, these regions may be attributed to small amounts of dynamic lithium density. The problem modeling these is due to two inherent shortcomings of the anharmonic DWF approach: first, the origins of the functions remain at the atoms' reference positions. This means that density far away from them is modeled less precisely. Second, the model may suffer from truncation effects. The equation presented above is the first part of a series expansion that is mathematically accurate only for an infinite number of terms. As the relatively low data-to-parameter ratio in powder diffraction does not allow for including too many intensity-dependent parameters in the refinement, artifacts like regions or spurious spikes of difference density (with a small absolute value) may occur.

3.1.2. Lithium-Diffusion Pathways. The reverse Fourier transform of an atom's DWF yields its PDF $F(\mathbf{u})$ of having the atom displaced by $\mathbf{u}$ from its reference position. (In the case of the Gram–Charlier expansion, the PDF is described analytically using Hermite polynomials.) Summing over the occupancy-

weighted PDFs of one kind of atom leads to the *joint PDF* describing the total probability density $F_j(\mathbf{u})$ of finding a displaced atom at a certain position within an area of interest.

The features of the found joint lithium PDF of several neighboring ions are very similar for the same lithium content at different temperatures. At 700 °C, the maxima of (time-averaged) probability density are just "smeared" over a somewhat larger volume, indicating (as is expected) a higher mobility of lithium ions. In contrast, the differences between the PDFs for different lithium contents at the same temperature are well pronounced. (Figure 3 shows the isosurface for a relatively low absolute value of the joint PDF to make features more easily visible.) For $x = 0.7$, the individual PDF seems nearly rotationally symmetric with respect to the c axis. Small
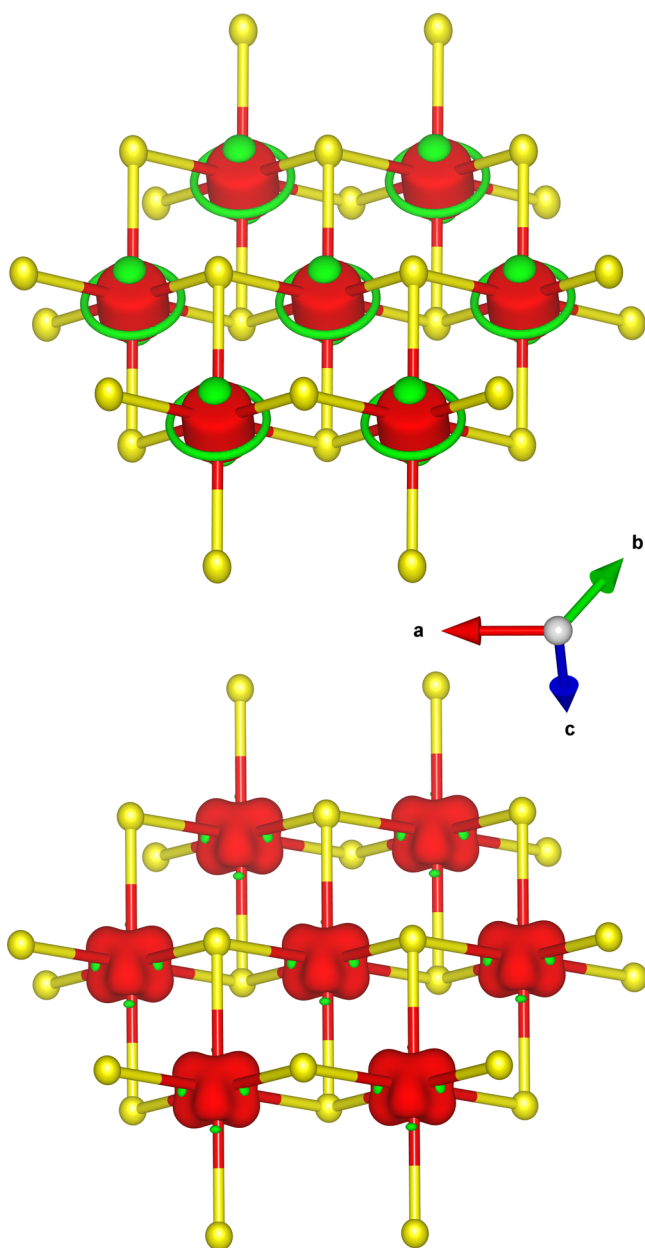
Figure 3. Joint PDF of several lithium ions in $Li_{0.7}TiS_2$ (top) and $Li_{0.9}TiS_2$ (bottom) at 700 °C. Yellow: sulfide ions as ellipsoids of 50% probability, red and green: isosurfaces for positive and negative lithium PDF of $F_j(\mathbf{u}) = \pm 0.07 \times 10^{-6}$ pm^{-3}, respectively.

rims of negative probability density, presumably being truncation artifacts (see above), surround the lithium ions in their layer. This hints at nearly isotropic diffusion within the layer along slightly curved pathways. For $x = 0.9$ on the other hand, lobes of probability-density sprawling into the tetrahedral voids between sulfide ions are clearly discernible. This indicates that the voids are part of a possible diffusion pathway.

To corroborate the conclusions drawn from the experimental data, we also analyzed the scattering-length densities using the maximum-entropy method (MEM). The latter is a versatile approach to the estimation of a model from a limited amount of information by maximizing information entropy under constraints consistent with observed physical quantities.[51] In crystallography, the MEM deals with the scattering densities by giving the maximum variance of calculated structure factors within standard deviations of observed structure factors. In this way, structural information can be effectively extracted from the diffraction data and reflected on the resulting three-dimensional distributions of scattering-length densities. Additionally, termination artifacts are less pronounced in comparison with Fourier synthesis, thus resulting in lower noise. Because of these advantages, the MEM has become a well-established technique in the visualization of lithium-diffusion pathways.[52,53]

The MEM analysis of the scattering-length density (see Figure 4) suggests that the rims and spikes of nonpositive PDF found with the evaluation of anharmonic DWFs (see Figure 3) are indeed artifacts of modeling. Small lobes of negative scattering-length density stretching out toward the centers of tetrahedral voids are present, but no significant negative density is found in them, indicating that also the areas shown in Figure 2 may be truncation artifacts. For $Li_{0.7}TiS_2$, slightly bent connections between the areas attributed to individual neighboring lithium ions exist. For $Li_{0.9}TiS_2$, on the other hand, these do not appear until the isosurface value is lowered to $\rho_b = -0.003$ fm $\times 10^{-6}$ pm^{-3}, implying that low values of negative scattering-length density (and thus high values of lithium probability density) are much more localized at the lithium-ion positions.

On the basis of the joint PDF of the lithium ions, the MEM analysis, the questionable regions of negative scattering-length density in the tetrahedral voids, and previous computational work on 1T-Li_xTiS_2,[23] we investigated three possible pathways of lithium-ion diffusion (see Figure 5):

- from an occupied lithium position to a next-neighboring vacancy directly within the lithium layer (path $\mathbf{A_1}$),
- from an occupied lithium position to a second next-neighboring vacancy directly within the lithium layer, thereby crossing an edge of the hexagon of next-neighboring lithium ions (path $\mathbf{A_2}$), and
- from an occupied lithium position to a next-neighboring vacancy indirectly through the center of an adjacent tetrahedral void (path $\mathbf{B}$).

To assess the viability and activation barriers of these pathways (see Figures S5–S16, SI), OPPs $V(\mathbf{u})$ have been calculated from the joint PDFs. In this approach, every atom is treated as an individual Einstein oscillator subject to Boltzmann statistics in the classical limit $[kT \gg V(\mathbf{u})]$. The maximum of the OPP along a certain path is the activation energy E_m for the migration (not comprising the defect-creation energy).[54] Additionally, the ratios of migration probabilities along $\mathbf{A_1}$ and $\mathbf{B}$ could be estimated from the activation energies E_m or

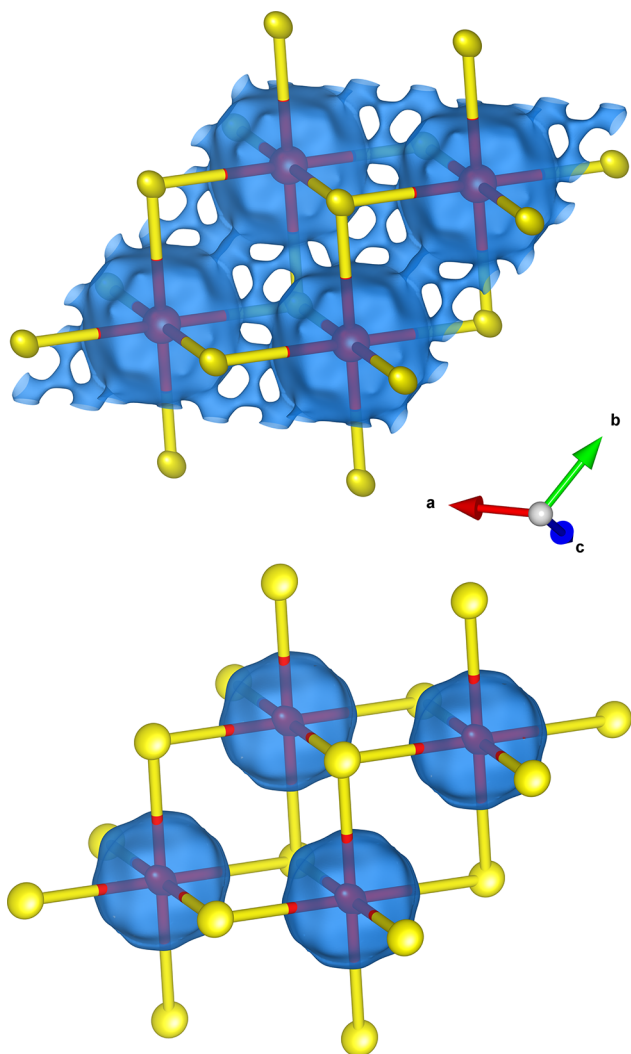**Figure 4.** Detail of MEM reconstructed scattering-length density in $Li_{0.7}TiS_2$ (top) and $Li_{0.9}TiS_2$ (bottom) at 600 °C showing only negative scattering-length density in and near the lithium layer. Yellow: sulfide ions, red: lithium ions, both as ellipsoids of 50% probability; blue: isosurface for $\rho_b = -0.008$ fm $\times$ 10^{-6} pm^{-3}.

Figure 5. Scheme of the evaluated diffusion pathways in $3R$-$LiTiS_2$. Green line: direct in-layer path to next neighboring site (A_1), blue line: direct in-layer path to second-next neighboring site (A_2), pink: indirect path through tetrahedral void (B). Ions with arbitrary radii, hexagon of next-neighboring lithium ions in black, edges of a representative tetrahedral void in white.

Figure 6. Section of the lithium OPP for $Li_{0.7}TiS_2$ at 600 °C in view of (010). Absolute Cartesian coordinates e_1 along the line between next-neighboring lithium positions and e_2 along the c axis. Contours from 0.1 to 1.0 eV (step: 0.1 eV) to 5.0 eV (step: 1.0 eV). Red, gray, and white areas: low, high, and infinitely high OPP, respectively; green solid and dotted line: A_1-like and direct A_1 pathway.

the minima of the PDF F_{min} using a simple Arrhenius-probability model

$$\frac{P(\mathbf{B})}{P(\mathbf{A_1})} = \exp\left(\frac{E_m(\mathbf{A_1}) - E_m(\mathbf{B})}{kT}\right) = \frac{F_{min}(\mathbf{B})}{F_{min}(\mathbf{A_1})}$$

The direct pathways in plane deviate somewhat from straight lines, the ones found being thus called "A_1-like" and "A_2-like". For $x = 0.7$, thin rims of negative PDF block straight in-plane paths. Being small, the former may well be considered model artifacts and ignored. Wavy (in c direction) A_1- or A_2-like paths, however, would have to pass the same area of high OPP thus leading to the same activation barrier (cf. Figure 6). For $x = 0.9$, larger areas of infinitely high OPP are found between the next- and second next-neighboring lithium positions. Only paths bent in c direction are found (cf. Figure 7). At 700 °C, these are additionally slightly shifted away from the centers of the lithium positions.

In all cases, the indirect pathways B cross areas of higher OPP compared to the A_1-like ones. They must be rather considered viable, but improbable paths as their maximal OPPs
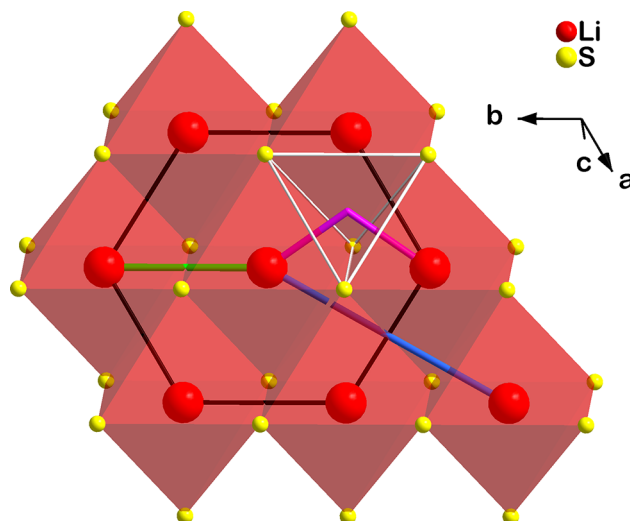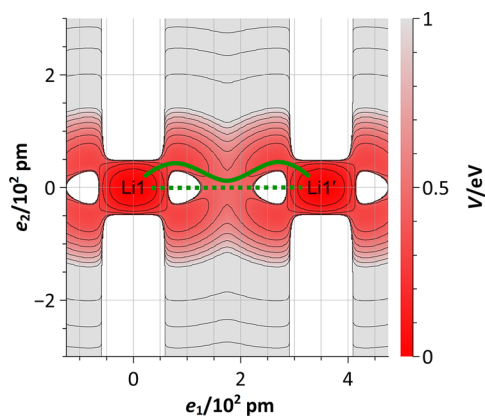
are upper bounds monotonically decreasing when approaching the A_1-like pathways that represent the lower bounds (cf. Figure 8). For comparison of OPPs, we have thus stuck to the initial definition of B comprising the center of a tetrahedral void.

The results of the OPP analyses are summarized in Table 4. In general, direct A_1-like paths are energetically preferred. The long-range A_2-like ones are significantly less favored, if viable at all. Pathways B exhibit even higher migration barriers leading to very small migration−probability ratios. However, the activation energies along B are probably overestimated because of the problems to model scattering-length density far from the ion positions (see above).

Strikingly, the barriers are much higher for $x = 0.9$ than for $x = 0.7$. As a consequence and in agreement with the MEM analysis (see above), the lithium ions become more strongly localized: the OPP further away from the reference position
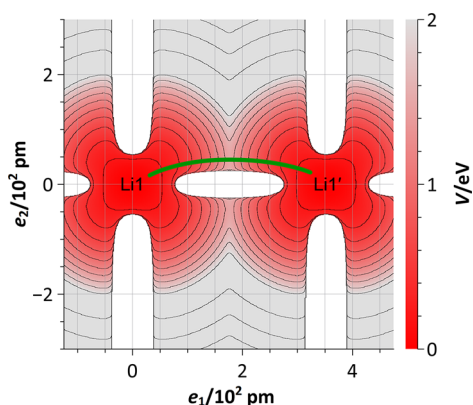
Figure 7. Section of the lithium OPP for $Li_{0.9}TiS_2$ at 600 °C in view of (010). Absolute Cartesian coordinates e_1 along the line between next-neighboring lithium positions and e_2 along the c axis. Contours from 0.2 to 2.0 eV (step: 0.2 eV) to 5.0 eV (step: 1.0 eV). Red, gray, and white areas: low, high, and infinitely high OPP, respectively; green line: A_1-like pathway.
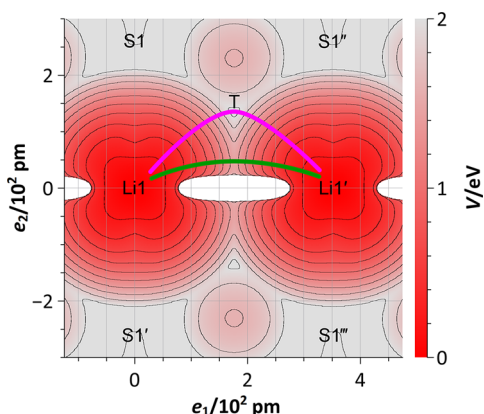

Figure 8. Section of the lithium OPP for $Li_{0.9}TiS_2$ at 600 °C in view of (0 4 30). Absolute Cartesian coordinates e_1 along the line between next-neighboring lithium ions and e_2 along the bond between Li1 and S1. Contours from 0.2 to 2.0 eV (step: 0.2 eV) to 5.0 eV (step: 1.0 eV). Red, gray, and white areas: low, high, and infinitely high OPP, respectively; green and pink line: A_1-like and B pathway; T: center of tetrahedral void.

Table 4. Measured Activation Energies E_m/eV for the Migration along Different Pathways and Ratios of Migration Probabilities

pathway	$Li_{0.7}TiS_2$		$Li_{0.9}TiS_2$	
	600 °C	700 °C	600 °C	700 °C
A_1-like	0.484(14)	0.56(2)	1.48(3)	1.56(3)
A_2-like	0.614(11)	0.692(17)	∞^a	1.75(3)
B	0.88(4)	0.83(2)	2.04(4)	2.23(5)
$P(B)/P(A_1)^b$	0.0052(3)	0.0399(11)	0.00058(3)	0.00034(2)

^{a}Blocked by large areas of infinitely high OPP. ^{b}See text.

rises, and the overall probability density to find an ion on its way to a defect decreases because defects are scarcer. The reason behind the unproportionally high barriers observed for $Li_{0.9}TiS_2$ is essentially the breakdown of the PDF-to-OPP formalism because of measurements below the classical limit and time- and space-averaging effects for insufficiently high defect concentrations (see Conclusions for an in-depth analysis). Furthermore, the values are similar but not equal at

different temperatures, being slightly (**B** in $Li_{0.9}TiS_2$: considerably) higher at 700 °C. The long A_2-like path in $Li_{0.9}TiS_2$, on the other hand, is only activated at all at elevated temperature. To elucidate the origin of the very high measured activation barriers for large x (e.g., artifacts or model failure are possible), we have employed computation. The method of choice for this kind of problem is DFT cNEB calculations, being state of the art and well-known for yielding realistic activation energies.

3.2. Computational Studies. *3.2.1. Octahedral vs Tetrahedral Lithium Sites in 3R-LiTiS₂.* To ensure correct optimization strategies, we have first studied the stability of 3R-LiTiS₂ with lithium ions occupying octahedral (O_h) or tetrahedral sites (T_d) in four different scenarios:

● All lithium ions occupy octahedral sites.
● One lithium ion is moved to a tetrahedral void from a neighboring octahedral site.
● One lithium ion is moved to a tetrahedral void from the adjacent layer (in c direction).
● One lithium ion is moved to a tetrahedral void from the layer after the next (in c direction).

While the Li−S distances are in all cases 2.59 Å (O_h) and 2.25−2.26 Å (T_d; cf. Figure S17, SI), we found that the all-octahedral coordination is by 0.28 eV/0.31 eV more stable than the occupation of an adjacent tetrahedral site/a tetrahedral site in a different layer, respectively. This finding is in accordance with the experimental observations for layered lithium titanium sulfides.[10,14,55] Therefore, we have considered lithium ions solely occupying octahedral sites for all following steps of our study.

3.2.2. Structure and Stability of 3R-Li$_x$TiS₂. The removal of one or four lithium ions from a $Li_{12}Ti_{12}S_{24}$ supercell yields compounds with lithium contents of $x \approx 0.92$ or 0.67, respectively. In the latter case, we have tested various models for the distribution of the lithium defects: all in the same layer, distributed over two or three layers. The most stable structure was obtained when distributing the four defects over three layers, in agreement with a previous theoretical study on 1T-Li$_x$TiS₂.[56] Therefore, we considered only this structure for further steps. The calculated structural properties such as lattice parameters and bond distances are summarized in Table 5.

Table 5. Calculated Lattice Parameters and Bond Lengths in 3R-Li$_x$TiS₂

x	a/pm	c/pm	d(Ti−S)/pm	d(Li−S)/pm
1.0[13]	351.0	1834.0	248.6	259.0
0.92	345.0	1857.0	248.2	259.8
0.67	344.0	1872.0	248.0	260.0

Compared to the experimental values for $x = 1.0$,[13] the calculated lattice parameter a is underestimated ($\Delta a = -2.3$ pm), and c is overestimated ($\Delta c = +26.5$ pm). The bond length d(Ti−S) is slightly overestimated (by 0.3%), and d(Li−S) is close to the experimental value. In our previous theoretical study,[13] we have applied the dispersion-corrected DFT approach (PBE-D) that led to a slightly improved c parameter compared to the experimental value ($\Delta c = -15$ pm), while a remained almost unchanged. Both d(Ti−S) and d(Li−S) are within a distance of 2 pm from the experimental bond lengths. These findings are in line with our previous investigation on 1T-LiTiS₂.[23] Therefore, we have adopted the uncorrected PBE
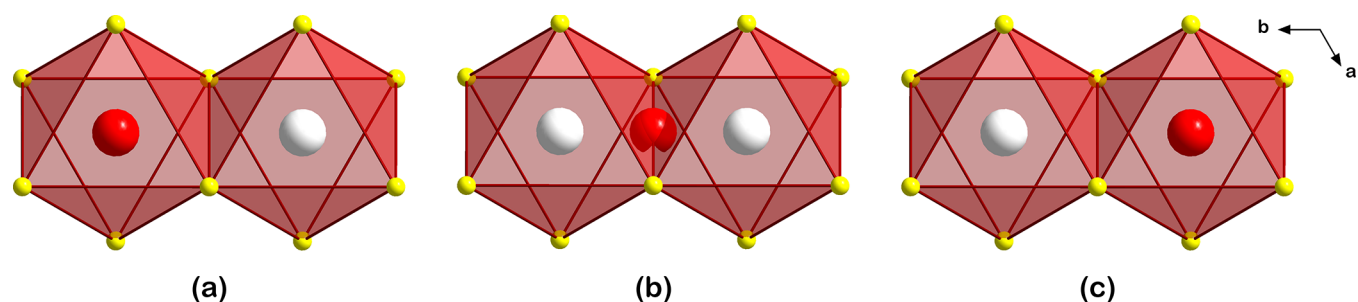
Figure 9. Lithium-ion migration along pathway A_1 (view along $[001]$). Initial state (a), transition state with lithium ion in center of shared octahedron edge (b), and final state (c). Yellow: sulfide ions, red: lithium ions, white: lithium defects.
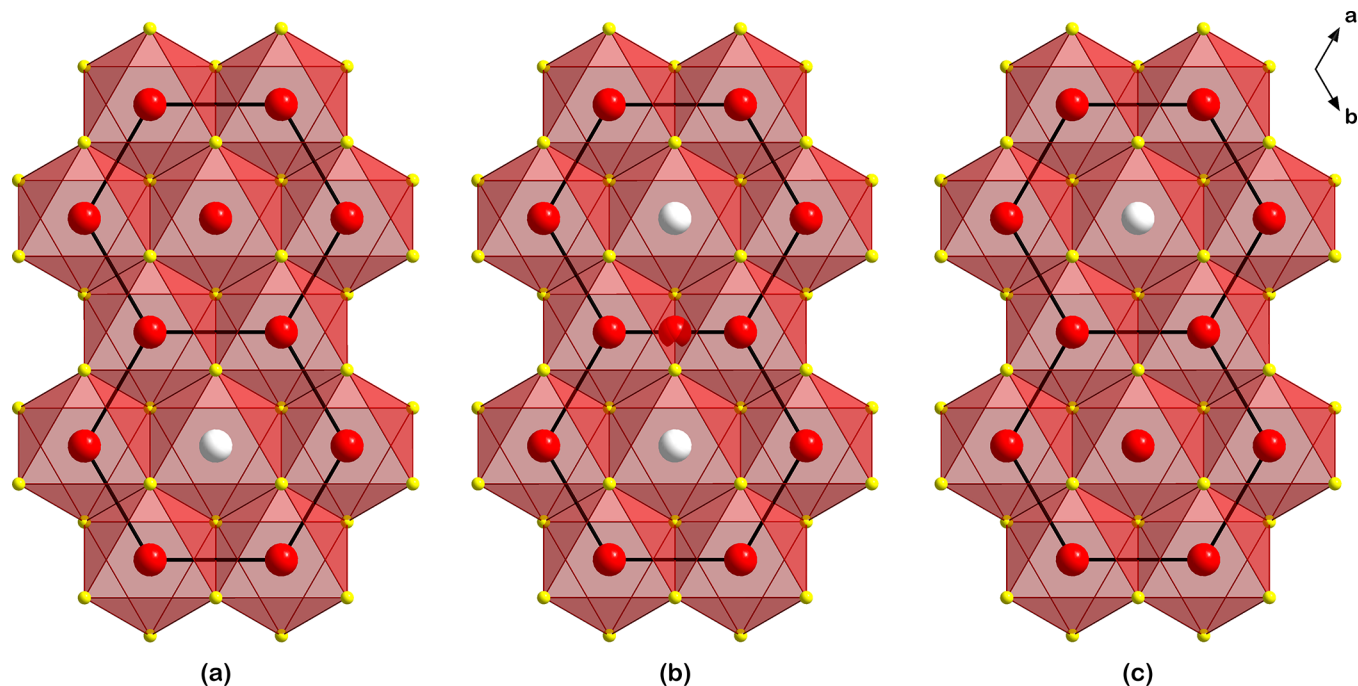

Figure 10. Lithium-ion migration along pathway A_2 (view along $[001]$). Initial state (a), transition state with lithium ion in the center of a shared octahedron edge (b), and final state (c). Yellow: sulfide ions, red: lithium ions, white: lithium defects.

approach for the subsequent calculations of defects and diffusion.

Better agreement with the experimental structural parameters (cf. Tables 1 and 3), as compared to $x = 1.0$, is obtained for $x = 0.92$ and 0.67. The lattice parameter a is only slightly underestimated ($\Delta a = -7$ and -6 pm for $x = 0.92$ and 0.67, respectively), and c is well in accordance with the experiment ($\Delta c = +1$ pm and $+6$ pm for $x = 0.92$ and 0.67, respectively). Eventually, the calculated Ti–S and Li–S bond distances have converged to the measured values within ± 2 pm.

3.2.3. Lithium-Diffusion Pathways in 3R-$Li_{0.92}TiS_2$. Direct migration of a lithium ion to an (previously created) adjacent point-defect site (pathway A_1) occurs as depicted in Figure 9: Starting from its octahedral site (see Figure 9a), the migrating ion passes through the center of a shared octahedron-edge (this being the transition state; see Figure 9b) and finally reaches the former defect position being 3.45 Å from the start (see Figure 9c). The activation energy for this migration process in 3R-$Li_{0.92}TiS_2$ is $E_A = 0.46$ eV. It should be noted that our definition of E_A does not include the defect formation energy.

Migrating along pathway A_2, a lithium ion moves in plane to a vacant next-neighboring site at a distance of 5.98 Å (see Figure 10a–c). Although the distance between the starting position and destination is larger than that of pathway A_2, the environment is similar for both cases. During the migration process, the lithium ion moves through the face of its initial coordination octahedron, crosses a shared octahedron edge (transition state), and moves through the face of its final coordination octahedron. In the transition state, the two nearest lithium atoms are 1.73 Å away. The activation energy for this process is $E_A = 0.47$ eV, which is in the range of direct migration via A_1.

Lithium-ion migration between two adjacent octahedral sites can also occur via the adjacent tetrahedral void (pathway **B**, see Figure 11d–f). In the transition state, the migrating ion occupies the center of a tetrahedral void. Calculated activation barriers range between 0.75 and 0.82 eV and depend on the position of the lithium defect with respect to the migrating ion. We have considered three different situations:

- The defect is located on the same layer as the migrating ion at a distance of 3.45 Å.
- The defect is located on the next layer (in c direction) at a distance of 6.50 Å.
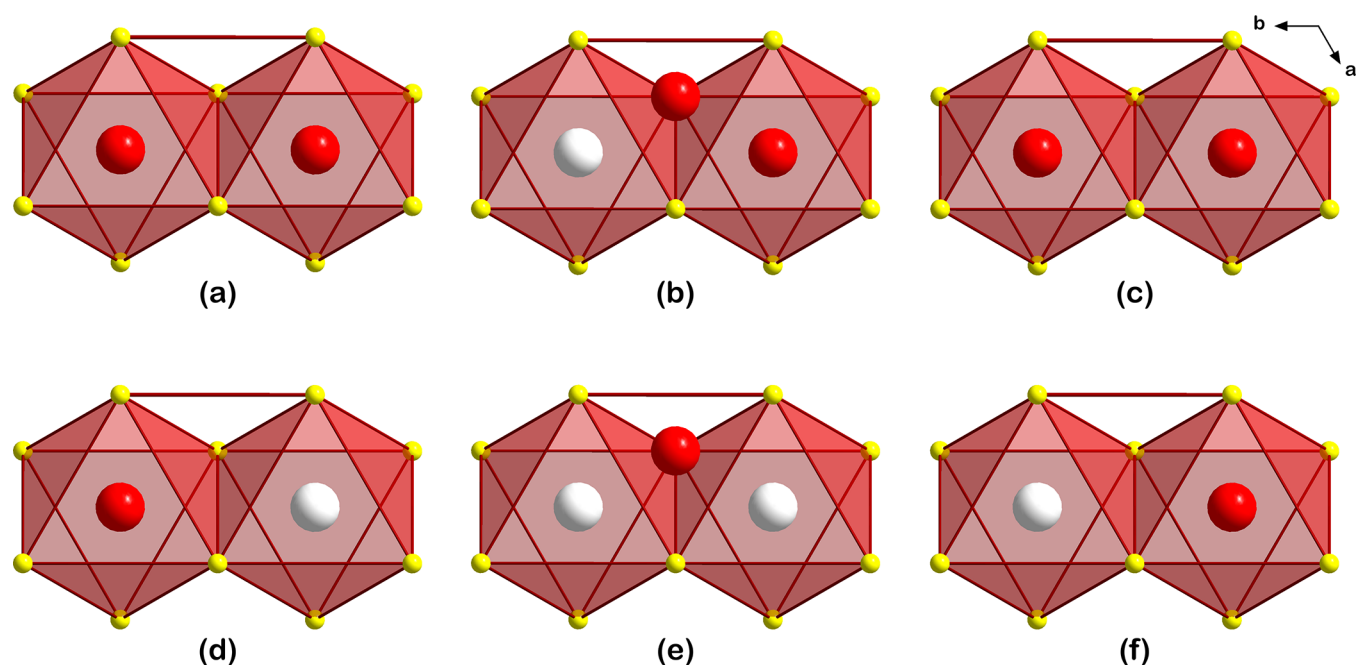- The defect is located on the layer after the next (in c direction) at a distance of 12.53 Å.

Figure 11. Lithium migration along pathway **B** (view along [001]). Initial state (a), transition state with lithium ion in the center of the tetrahedral void (b), and final state (c) for a "local hopping" process; initial state (d), transition state with lithium ion in the center of the tetrahedral void (e), and final state (f) for migration to an adjacent defect. Yellow: sulfide ions, red: lithium ions, white: lithium defects.

The results (see Table 6) indicate that the location of a lithium defect near the migration pathway facilitates diffusion. It

Table 6. Calculated Activation Energies E_A/eV for Lithium Migration in $Li_{11}Ti_{12}S_{24}$ ($Li_{0.92}TiS_2$)

pathway	defect position	E_A/eV
A_1	adjacent site	0.46
A_2	next-neighboring site	0.47
B	same layer	0.75
	next layer	0.80
	layer after the next	0.82

should be noted that the second and the third model examined for pathway **B** refer to "local hopping"; i.e., the lithium ion migrates into a tetrahedral void and back to its former position as there is no other adjacent vacancy available (see Figure 11a–c).

3.2.4. Lithium-Diffusion Pathways in 3R-$Li_{0.67}TiS_2$. Lithium migration diffusion processes in 3R-$Li_{0.67}TiS_2$ are strongly affected by the location of the four vacancies in the $Li_{(12-4)}Ti_{12}S_{24}$ supercell. For the pathways A_1 and A_2, we have considered two cases:

● Two lithium defects are located on the same layer as the migrating ion at a nearest distance of 3.45 Å creating a divacancy in the pathway. The third and fourth defects are located on the next layer and the layer after the next at 6.50 and 12.40 Å, respectively.

● One lithium defect is located on the same layer as the migrating ion at a distance of 3.45 Å. Two defects are located on the next layer at 6.50 Å, and the fourth one is located on the layer after the next at 12.40 Å.

In the first case, in which the end point of the hop belongs to a divacancy, activation energies of 0.44 eV/0.42 eV were calculated for A_1/A_2, respectively. In contrast, relatively high barriers result in the case of migration via an isolated vacancy

(0.56 eV/0.69 eV). This indicates that lithium diffusion is easier when many defects close to the migrating ion are present.

For lithium-ion migration along pathway **B**, a broad variety of defect configurations are possible (cf. Table 7). The activation

Table 7. Calculated Activation Energies E_A/eV for Lithium Migration in $Li_8Ti_{12}S_{24}$ ($Li_{0.67}TiS_2$)

pathway	defect distribution	nearest defect position	E_A/eV
A_1	2 × same layer, 1 × next layer, 1 × layer after next		0.44
	1 × same layer, 2 × next layer, 1 × layer after next		0.56
A_2	2 × same layer, 1 × next layer, 1 × layer after next		0.42
	1 × same layer, 2 × next layer, 1 × layer after next		0.69
B	1 × same layer, 2 × next layer, 1 × layer after next	in pathway (3.45 Å)	0.45
		close (3.45 Å)	0.53
		far (6.50 Å)	0.84
	1 × same layer, 3 × next layer	close (3.45 Å)	0.54
		far (6.50 Å)	0.81
	2 × same layer, 2 × next layer	close (3.45 Å)	0.51
		far (6.50 Å)	0.73
	3 × same layer, 1 × next layer	close (3.45 Å)	0.51
	4 × next layer	far (6.50 Å)	0.74
	2 × next layer, 2 × layer after next	very far (12.40 Å)	0.89

energies E_A calculated with these models range between 0.45 and 0.53 eV, if the defects are located near the migrating ion (location of divacancy within 3.45 Å), and between 0.73 and 0.84 eV, if the defects are far from the migrating ion (at least 6.50 Å). With even larger distances (at 12.40 Å), an activation barrier of 0.89 eV is found.

3.2.5. Summary. According to our computational investigations, the calculated activation energies E_A for migration via pathway A_1 are 0.44−0.56 eV ($x = 0.67$) and 0.46 eV ($x = 0.92$). For migration via A_2, they are 0.42−0.69 eV ($x = 0.67$) and 0.47 eV ($x = 0.92$). Jump processes including the adjacent tetrahedral voids (pathway B) have activation barriers of 0.45−0.89 eV ($x = 0.67$) and 0.75−0.82 eV ($x = 0.92$). These findings suggest that

● the pathways A_1 have the smallest activation barriers and are thus most preferable, followed by the pathways A_2 and B;

● due to a lower defect concentration and therefore increased electrostatic repulsion between migrating and surrounding lithium ions, the activation barriers for all pathways are larger in 3R-$Li_{0.92}TiS_2$ than in 3R-$Li_{0.67}TiS_2$;

● changes in the defect distribution model have a large impact on the calculated barriers. In all cases, the location of divacancies in the migration path produces the smallest activation barriers (0.44 eV for A_1, 0.42 eV for A_2, and 0.45−0.53 eV for B). This is due to less electrostatic interaction of the lithium ion during divacancy as compared to single-vacancy migration. These findings are in line with the ones already made in layered transition-metal oxides (Li_xCoO_2)[57] and sulfides (Li_xTiS_2),[24] where the dominant diffusion-mediated complex is a divacancy.

As there is no experimental and theoretical study available for the lithium diffusion in 3R-Li_xTiS_2, we compare our results to the available data on 1T-Li_xTiS_2. Some of us have studied lithium diffusion in 1T-Li_xTiS_2 theoretically via pathways B and A_1.[21,23] These investigations produced activation energies of 0.40 and 0.75 eV for pathway B for $x = 0.67$ and 1, respectively, as well as 0.45 eV for pathway A_1 for $x = 0.88$. Van der Ven et al. have found activation energies of 0.42−0.65 eV for a divacancy and 0.70 eV for a single-vacancy mechanism along pathway B in 1T-$LiTiS_2$.[24] Interestingly, despite dealing with two different polymorphs, our results are in good agreement with these values. They also comply to the experimental barrier of 0.41 eV for 1T-$Li_{0.7}TiS_2$ as measured with NMR methods.[58,59]

4. CONCLUSIONS

Qualitatively, computational and experimental data (see Tables 4, 6, and 7) show the same trends: The short pathways A_1 have the lowest activation barrier, followed by the longer ones A_2 and the indirect pathways B. We conclude that the lithium-ion diffusion in plane is the principal migration mechanism whereby jumps to directly adjacent defects are preferred over those to next-neighboring ones. Quantitatively, however, only the results for $x = 0.7$ are reconcilable, although the experimental activation energies are systematically higher than the calculated ones: ca. 0.5, 0.6, and 0.8 eV along the pathways A_1, A_2, and B, respectively. For $x = 0.9$, the measured values are, however, at least thrice as high as the computed ones.

In order to investigate this inconsistency, we have performed test calculations for $x \approx 0.89$ with a larger supercell ($Li_{24}Ti_{27}S_{54}$). As the resulting activation barriers were only by 0.04 and 0.05 eV higher along A_1 and A_2, respectively, the choice of the supercell size cannot be responsible for the discrepancy. On the other hand, another test calculation for a local hop in 3R-$Li_{0.92}TiS_2$ (original supercell) with all defects far away from the migrating lithium ion yielded a significantly higher energy increase of 1.0 eV when the lithium ion was held fixed at the transition-state position with a nearby defect along pathway A_1. This finding underlines the importance of nearby lithium vacancies for efficient migration. Of course, in this configuration, the lithium ion would fall back into its initial position, if the geometrical constraints were removed, and no migration process would occur.

The computational methods employed in this work provide activation barriers that have been shown to be, in general, directly comparable to and in good agreement with those gained from NMR relaxation measurements or impedance spectroscopy, i.e., experiments analyzing microscopic hopping processes. This has, e.g., been shown for lithium-ion diffusion in 1T-$LiTiS_2$,[21,23] Li_2O and the system Li_2O−B_2O_3,[60−66] α-$LiVF_6$,[67] and LiC_6.[68] In these cases, single jumps from the equilibrium position to an unoccupied site are examined, yielding the potential landscape as experienced by an *individual* lithium ion with one or more defects nearby. Neutron diffraction, on the other hand, is a method averaging over time (usually several hours) and space (in this case, every single lithium position in the bulk). The activation barriers derived from OPPs are thus an average of the potential landscape that *every* lithium ion experiences—be it with vacancies nearby or not. Consequently, if the defect concentration is low (like in 3R-$Li_{0.9}TiS_2$), only a minority of individual ions can migrate to an adjacent site and will do so. The resulting average barrier from OPP data will then be much higher than the one derived from computation.

In this context, a drawback inherent to the PDF-to-OPP formalism should be recalled: It is only valid at the classical limit $[kT \gg V(\mathbf{u})]$. At a temperature of 700 °C, this means that already $E_m \geq 0.08$ eV are biased toward too high values. This limitation is easily rationalized: If the thermal energy present in the system is not sufficiently high, only few individual ions will be able to overcome the (finite) activation barrier for a certain pathway. As the majority of ions will be confined to the near environment of their equilibrium positions, there will be little "smearing" of space-averaged lithium scattering-length density as conveyed by the observed DWF. The apparent OPP barrier, as calculated from the derived PDF, will then be too (in the extreme, infinitely) high—just due to the lack of thermal energy to scan the potential landscape.

Because of these reasons, we attribute the systematically higher experimental activation barriers to (a) measurements below the classical limit and (b) time- and space-averaging effects for insufficiently high defect concentrations, especially in the case of 3R-$Li_{0.9}TiS_2$.

■ ASSOCIATED CONTENT

Ⓢ Supporting Information

Diffractograms, PDF contour plots, details of calculated structures, and CIFs. Further details of the crystal structure investigations may be obtained from Fachinformationszentrum Karlsruhe, 76344 Eggenstein-Leopoldshafen, Germany (fax: +49 7247 808−666; e-mail: crysdata@fiz-karlsruhe.de, http://www.fiz-karlsruhe.de/request_for_deposited_data.html on quoting the deposition numbers CSD-429110 to CSD-429113). The Supporting Information is available free of charge on the ACS Publications website at DOI: 10.1021/acs.jpcc.5b01166.

■ AUTHOR INFORMATION

Corresponding Author

*E-mail: dennis.wiedemann@chem.tu-berlin.de. Phone: +49 30 314-26178. Fax: +49 30 314-79656.

■ REFERENCES

(1) Thompson, A. H.; Gamble, F. R.; Symon, C. R. The Verification of the Existence of TiS_2. *Mater. Res. Bull.* **1975**, *10*, 915−919.

(2) Lévy, F., Ed. *Intercalated Layered Materials*; D. Reidel Publishing: Dordrecht, Netherlands, 1979.

(3) Whittingham, M. S. Chemistry of Intercalation Compounds: Metal Guests in Chalcogenide Hosts. *Prog. Solid State Chem.* **1978**, *12*, 41−99.

(4) Whittingham, M. S.; Jacobson, A. J., Eds. *Intercalation Chemistry*; Academic Press: New York, USA, 1982.

(5) Whittingham, M. S. Electrical Energy Storage and Intercalation Chemistry. *Science* **1976**, *192*, 1126−1127.

(6) Tarascon, J.-M.; Armand, M. Issues and Challenges Facing Rechargeable Lithium Batteries. *Nature* **2001**, *414*, 359−367.

(7) Oftedal, I. Röntgenographische Untersuchungen von SnS_2, TiS_2, $TiSe_2$, $TiTe_2$. *Z. Phys. Chem., Stoechiom. Verwandtschaftsl.* **1928**, *134*, 301−310.

(8) Schöllhorn, R.; Payer, A. c-TiS_2, a New Modification of Titanium Disulfide with Cubic Structure. *Angew. Chem., Int. Ed. Engl.* **1985**, *24*, 67−68.

(9) Lightfoot, P.; Krok, F.; Nowinski, J. L.; Bruce, P. G. Structure of the Cubic Intercalate Mg_xTiS_2. *J. Mater. Chem.* **1992**, *2*, 139−140.

(10) Dahn, J. R.; McKinnon, W. R.; Haering, R. R.; Buyers, W. J. L.; Powell, B. M. Structure Determination of Li_xTiS_2 by Neutron Diffraction. *Can. J. Phys.* **1980**, *58*, 207−213.

(11) Sinha, S.; Murphy, D. W. Lithium Intercalation in Cubic TiS_2. *Solid State Ionics* **1986**, *20*, 81−84.

(12) Colbow, K. M.; Dahn, J. R.; Haering, R. R. The 3R Phase of Li_xTiS_2. *J. Power Sources* **1989**, *26*, 301−307.

(13) Nakhal, S.; Lerch, M.; Koopman, J.; Islam, M. M.; Bredow, T. Crystal Structure of 3R-$LiTiS_2$ and Its Stability Compared to Other Polymorphs. *Z. Anorg. Allg. Chem.* **2013**, *639*, 2822−2825.

(14) Wiedemann, D.; Nakhal, S.; Senyshyn, A.; Bredow, T.; Lerch, M. The High-Temperature Transformation from 1T- to 3R-Li_xTiS_2 (x = 0.7, 0.9) as Observed *In Situ* with Neutron Powder Diffraction. *Z. Phys. Chem.* **2015**, DOI: 10.1515/zpch-2014-0659.

(15) Wilkening, M. The 3R Modification of Li_xTiS_2 — Insights into Local Electronic Structures from High-Temperature *In Situ* NMR Spectroscopy. *Philos. Mag.* **2015**, *95*, 861−868.

(16) Islam, M. S.; Fisher, C. A. J. Lithium and Sodium Battery Cathode Materials: Computational Insights into Voltage, Diffusion and Nanostructural Properties. *Chem. Soc. Rev.* **2014**, *43*, 185−204.

(17) Filsø, M. Ø.; Turner, M. J.; Gibbs, G. V.; Adams, S.; Spackman, M. A.; Iversen, B. B. Visualizing Lithium-Ion Migration Pathways in Battery Materials. *Chem.—Eur. J.* **2013**, *19*, 15535−15544.

(18) Ganesh, P.; Kim, J.; Park, C.; Yoon, M.; Reboredo, F. A.; Kent, P. R. C. Binding and Diffusion of Lithium in Graphite: Quantum Monte Carlo Benchmarks and Validation of van der Waals Density Functional Methods. *J. Chem. Theory Comput.* **2014**, *10*, 5318−5323.

(19) Bredow, T.; Heitjans, P.; Wilkening, M. Electric Field Gradient Calculations for Li_xTiS_2 and Comparison with ^7Li NMR Results. *Phys. Rev. B: Condens. Matter Mater. Phys.* **2004**, *70*, 115111.

(20) Tibbetts, K.; Miranda, C. R.; Meng, Y. S.; Ceder, G. An *Ab Initio* Study of Lithium Diffusion in Titanium Disulfide Nanotubes. *Chem. Mater.* **2007**, *19*, 5302−5308.

(21) Bensch, W.; Bredow, T.; Ebert, H.; Heitjans, P.; Indris, S.; Mankovsky, S.; Wilkening, M. Li Intercalation and Anion/Cation Substitution of Transition Metal Chalcogenides: Effects on Crystal Structure, Microstructure, Magnetic Properties and Li^+ Ion Mobility. *Prog. Solid State Chem.* **2009**, *37*, 206−225.

(22) Bhattacharya, J.; Van der Ven, A. First-Principles Study of Competing Mechanisms of Nondilute Li Diffusion in Spinel Li_xTiS_2. *Phys. Rev. B: Condens. Matter Mater. Phys.* **2011**, *83*, 144302.

(23) Islam, M. M.; Bredow, T. Theoretical Investigation of Migration Pathways for Li Diffusion in h-$LiTiS_2$. *Z. Phys. Chem.* **2012**, *226*, 449−459.

(24) Van der Ven, A.; Thomas, J. C.; Xu, Q.; Swoboda, B.; Morgan, D. Nondilute Diffusion from First Principles: Li Diffusion in Li_xTiS_2. *Phys. Rev. B: Condens. Matter Mater. Phys.* **2008**, *78*, 104306.

(25) Hoelzel, M.; Senyshyn, A.; Juenke, N.; Boysen, H.; Schmahl, W.; Fuess, H. High-Resolution Neutron Powder Diffractometer SPODI at Research Reactor FRM II. *Nucl. Instrum. Methods Phys. Res., Sect. A* **2012**, *667*, 32−37.

(26) Bergerhoff, G.; Brown, I. D. Inorganic Crystal Structure Database. In *Crystallographic Databases*; Allen, F. H., Bergerhoff, G., Sievers, R., Eds.; International Union of Crystallography: Chester, U.K., 1987; pp 77−95.

(27) Petříček, V.; Dušek, M.; Palatinus, L. Crystallographic Computing System JANA2006: General Features. *Z. Kristallogr. − Cryst. Mater.* **2014**, *229*, 345−352.

(28) Thompson, P.; Cox, D. E.; Hastings, J. B. Rietveld Refinement of Debye-Scherrer Synchrotron X-Ray Data from Al_2O_3. *J. Appl. Crystallogr.* **1987**, *20*, 79−83.

(29) Bérar, J.-F.; Baldinozzi, G. Modeling of Line-Shape Asymmetry in Powder Diffraction. *J. Appl. Crystallogr.* **1993**, *26*, 128−129.

(30) March, A. Mathematische Theorie der Regelung nach der Korngestalt bei Affiner Deformation. *Z. Kristallogr., Kristallgeom., Kristallphys., Kristallchem.* **1932**, *81*, 285−297.

(31) Dollase, W. Correction of Intensities for Preferred Orientation in Powder Diffractometry: Application of the March Model. *J. Appl. Crystallogr.* **1986**, *19*, 267−272.

(32) Kuhs, W. Generalized Atomic Displacements in Crystallographic Structure Analysis. *Acta Crystallogr., Sect. A: Found. Crystallogr.* **1992**, *48*, 80−98.

(33) Wiedemann, D. *CalcOPP: Calculation of 2D OPP from PDF Data* [Online], version 1.5; http://www.tu-berlin.de/?id=136063 (accessed August 2013).

(34) Brandenburg, K.; Putz, H. *Diamond: Crystal and Molecular Structure Visualization* [Online], version 3.2; http://www.crystalimpact.com/diamond (accessed November 2014).

(35) Momma, K.; Izumi, F. *VESTA 3* for Three-Dimensional Visualization of Crystal, Volumetric and Morphology Data. *J. Appl. Crystallogr.* **2011**, *44*, 1272−1276.

(36) Vasilef, I. *QtiPlot: Data Analysis and Scientific Visualisation* [Online], version 0.9.9; http://www.qtiplot.com/ (accessed June 2014).

(37) Rodríguez-Carvajal, J. Recent Advances in Magnetic Structure Determination by Neutron Powder Diffraction. *Phys. B: Condens. Matter* **1993**, *192*, 55−69.

(38) Izumi, F.; Dilanian, R. A. Structure Refinement Based on the Maximum-Entropy Method from Powder Diffraction Data. In *Recent Research Developments in Physics*; Pandalai, S. G., Ed.; Transworld Research Network: Trivandrum, India, 2002; Vol. 3, pp 699−726.

(39) Perdew, J. P.; Burke, K.; Ernzerhof, M. Errata: Generalized Gradient Approximation Made Simple [*Phys. Rev. Lett.* 77, 3865 (1996)]. *Phys. Rev. Lett.* **1997**, *78*, 1396−1396.

(40) Perdew, J. P.; Burke, K.; Ernzerhof, M. Generalized Gradient Approximation Made Simple. *Phys. Rev. Lett.* **1996**, *77*, 3865−3868.

(41) Kresse, G.; Hafner, J. *Ab Initio* Molecular Dynamics for Liquid Metals. *Phys. Rev. B: Condens. Matter Mater. Phys.* **1993**, *47*, 558−561.

(42) Kresse, G.; Hafner, J. *Ab Initio* Molecular Dynamics for Open-Shell Transition Metals. *Phys. Rev. B: Condens. Matter Mater. Phys.* **1993**, *48*, 13115−13118.

(43) Kresse, G.; Hafner, J. *Ab Initio* Molecular-Dynamics Simulation of the Liquid-Metal−Amorphous-Semiconductor Transition in Germanium. *Phys. Rev. B: Condens. Matter Mater. Phys.* **1994**, *49*, 14251−14269.

(44) Kresse, G.; Joubert, D. From Ultrasoft Pseudopotentials to the Projector Augmented-Wave Method. *Phys. Rev. B: Condens. Matter Mater. Phys.* **1999**, *59*, 1758−1775.

(45) Blöchl, P. E. Projector Augmented-Wave Method. *Phys. Rev. B: Condens. Matter Mater. Phys.* **1994**, *50*, 17953−17979.

(46) Monkhorst, H. J.; Pack, J. D. Special Points for Brillouin-Zone Integrations. *Phys. Rev. B: Solid State* **1976**, *13*, 5188−5192.

(47) Grimme, S.; Antony, J.; Ehrlich, S.; Krieg, H. A Consistent and Accurate *Ab Initio* Parametrization of Density Functional Dispersion Correction (DFT-D) for the 94 Elements H-Pu. *J. Chem. Phys.* **2010**, *132*, 154104.

(48) Grimme, S.; Ehrlich, S.; Goerigk, L. Effect of the Damping Function in Dispersion Corrected Density Functional Theory. *J. Comput. Chem.* **2011**, *32*, 1456−1465.

(49) Jónsson, H.; Mills, G.; Jacobsen, K. W. Nudged Elastic Band Method for Finding Minimum Energy Paths of Transitions. In *Classical and Quantum Dynamics in Condensed Phase Simulations*; Berne, B. J., Ciccotti, G., Coker, D. F., Eds.; World Scientific Publishing: Singapore, Singapore, 1998; pp 385−404.

(50) Trueblood, K. N.; Bürgi, H.-B.; Burzlaff, H.; Dunitz, J. D.; Gramaccioli, C. M.; Schulz, H. H.; Shmueli, U.; Abrahams, S. C. Atomic Displacement Parameter Nomenclature. Report of a Subcommittee on Atomic Displacement Parameter Nomenclature. *Acta Crystallogr., Sect. A: Found. Crystallogr.* **1996**, *52*, 770−781.

(51) Izumi, F. Beyond the Ability of Rietveld Analysis: MEM-Based Pattern Fitting. *Solid State Ionics* **2004**, *172*, 1−6.

(52) Senyshyn, A.; Boysen, H.; Niewa, R.; Banys, J.; Kinka, M.; Burak, Y.; Adamiv, V.; Izumi, F.; Chumak, I.; Fuess, H. High-Temperature Properties of Lithium Tetraborate $Li_2B_4O_7$. *J. Phys. D: Appl. Phys.* **2012**, *45*, 175305.

(53) Yashima, M. Diffusion Pathway of Mobile Ions and Crystal Structure of Ionic and Mixed Conductors − A Brief Review. *J. Ceram. Soc. Jpn.* **2009**, *117*, 1055−1059.

(54) Boysen, H. The Determination of Anharmonic Probability Densities from Static and Dynamic Disorder by Neutron Powder Diffraction. *Z. Kristallogr.* **2003**, *218*, 123−131.

(55) Prigge, C.; Müller-Warmuth, W.; Schöllhorn, R. NMR Studies of Lithium Intercalated in the Host Compounds $1T\text{-}TiS_2$, $c\text{-}TiS_2$ and VSe_2. *Z. Phys. Chem.* **1995**, *189*, 153−168.

(56) En-Yong, J.; Qing-Gong, S.; Jian-Hai, K. Staging Effects on the Structural and Energetic Properties of Fast Ionic Conductor Li_xTiS_2. *Acta Phys. Sin.* **2008**, *57*, 3093−3099.

(57) Van der Ven, A.; Ceder, G.; Asta, M.; Tepesch, P. D. First-principles Theory of Ionic Diffusion with Nondilute Carriers. *Phys. Rev. B: Condens. Matter Mater. Phys.* **2001**, *64*, 184307.

(58) Wilkening, M.; Küchler, W.; Heitjans, P. From Ultraslow to Fast Lithium Diffusion in the 2D Ion Conductor $Li_{0.7}TiS_2$ Probed Directly by Stimulated-Echo NMR and Nuclear Magnetic Relaxation. *Phys. Rev. Lett.* **2006**, *97*, 065901.

(59) Wilkening, M.; Heitjans, P. Li Jump Process in $h\text{-}Li_{0.7}TiS_2$ Studied by Two-Time ^{7}Li Spin-Alignment Echo NMR and Comparison with Results on Two-Dimensional Diffusion from Nuclear Magnetic Relaxation. *Phys. Rev. B: Condens. Matter Mater. Phys.* **2008**, *77*, 024311.

(60) Heitjans, P.; Indris, S. Diffusion and Ionic Conduction in Nanocrystalline Ceramics. *J. Phys.: Condens. Matter* **2003**, *15*, R1257−R1289.

(61) Islam, M. M.; Bredow, T.; Heitjans, P. The Ionic Conductivity in Lithium-Boron Oxide Materials and Its Relation to Structural,

Electronic and Defect Properties: Insights from Theory. *J. Phys.: Condens. Matter* **2012**, *24*, 203201.

(62) Islam, M. M.; Bredow, T.; Heitjans, P. Formation and Mobility of Li Point Defects in $LiBO_2$: A First-Principles Investigation. *J. Phys. Chem. C* **2011**, *115*, 12343−12349.

(63) Islam, M. M.; Bredow, T. Density Functional Theory Study for the Stability and Ionic Conductivity of Li_2O Surfaces. *J. Phys. Chem. C* **2009**, *113*, 672−676.

(64) Islam, M. M.; Bredow, T.; Indris, S.; Heitjans, P. Enhanced Conductivity at the Interface of $Li_2O:B_2O_3$ Nanocomposites: Atomistic Models. *Phys. Rev. Lett.* **2007**, *99*, 145502.

(65) Islam, M. M.; Bredow, T.; Minot, C. Ionic Conductivity of $Li_2B_4O_7$. *J. Phys. Chem. B* **2006**, *110*, 17518−17523.

(66) Islam, M. M.; Bredow, T.; Minot, C. Theoretical Analysis of Structural, Energetic, Electronic, and Defect Properties of Li_2O. *J. Phys. Chem. B* **2006**, *110*, 9413−9420.

(67) Islam, M. M.; Wilkening, M.; Heitjans, P.; Bredow, T. Insights into Li^+ Migration Pathways in $\alpha\text{-}Li_3VF_6$: A First-Principles Investigation. *J. Phys. Chem. Lett.* **2012**, *3*, 3120−3124.

(68) Thinius, S.; Islam, M. M.; Heitjans, P.; Bredow, T. Theoretical Study of Li Migration in Lithium−Graphite Intercalation Compounds with Dispersion-Corrected DFT Methods. *J. Phys. Chem. C* **2014**, *118*, 2273−2280.